Antiferromagnetism and the emergence of frustration in the sawtooth lattice chalcogenide olivines $Mn_2SiS_{4-x}Se_x$ ($x = 0$–4)

H. Nhalil,[1] R. Baral,[2] B. O. Khamala,[2] A. Cosio,[2] S. R. Singamaneni,[2] M. Fitta,[3] D. Antonio,[4] K. Gofryk,[4] R. R. Zope,[2] T. Baruah,[2] B. Saparov,[1,*] and H. S. Nair[2,†]

[1]*Department of Chemistry and Biochemistry, University of Oklahoma, 101 Stephenson Parkway, Norman, Oklahoma 73019, USA*
[2]*Department of Physics, 500 West University Avenue, University of Texas, El Paso, Texas 79968, USA*
[3]*Institute of Nuclear Physics, Polish Academy of Sciences, 31-342 Kraków, Poland*
[4]*Idaho National Laboratory, Idaho Falls, Idaho 83415, USA*

(Received 3 March 2019; revised manuscript received 6 May 2019; published 24 May 2019)

The magnetism in the sawtooth lattice of Mn in the olivine chalcogenides, $Mn_2SiS_{4-x}Se_x$ ($x = 1$–4), is studied in detail by analyzing their magnetization, specific heat, and thermal conductivity properties and complemented with density functional theory calculations. The air-stable chalcogenides are antiferromagnets and show a linear trend in the transition temperature T_N as a function of Se content (x), which shows a decrease from $T_N \approx 86$ K for Mn_2SiS_4 to 66 K for Mn_2SiSe_4. Additional magnetic anomalies are revealed at low temperatures for all the compositions. Magnetization irreversibilities are observed as a function of x. The specific heat and the magnetic entropy indicate the presence of short-range spin fluctuations in $Mn_2SiS_{4-x}Se_x$. A spin-flop antiferromagnetic phase transition in the presence of applied magnetic field is present in $Mn_2SiS_{4-x}Se_x$, where the critical field for the spin flop increases from $x = 0$ towards 4 in a nonlinear fashion. Density functional theory calculations show that an overall antiferromagnetic structure with ferromagnetic coupling of the spins in the *ab* plane minimizes the total energy. The band structures calculated for Mn_2SiS_4 and Mn_2SiSe_4 reveal features near the band edges similar to those reported for Fe-based olivines suggested as thermoelectrics; however the experimentally determined thermal transport data do not support superior thermoelectric features. The transition from long-range magnetic order in Mn_2SiS_4 to short-range order and spin fluctuations in Mn_2SiSe_4 is explained using the variation of the Mn-Mn distances in the triangle units that constitutes the sawtooth lattice upon progressive replacement of sulfur with selenium. Overall, the results presented here point towards the role played by magnetic anisotropy and geometric frustration in the antiferromagnetic state of the sawtooth olivines.

DOI: 10.1103/PhysRevB.99.184434

I. INTRODUCTION

Complex magnetic excitations from frustrated lattices of magnetic atoms is an attractive topic in quantum correlated systems. The sawtooth antiferromagnetic chain has a frustrated topology of corner-sharing triangles of spins in which the ground state of the spin-half sawtooth chain is understood exactly [1–3]. A variety of ground states are predicted for the sawtooth lattice depending on the ratio of the exchange interaction strengths between the base-base and the base-vertex pairs [4–8]. The sawtooth systems attain importance in connection with the zero-energy flat-band modes similarly to the case of kagome lattices [9,10] and are valuable as potential materials for magnonics [11]. Experimental studies on sawtooth lattices are limited in number; some examples are the delafossites, olivines, and germanates [12–15]. In this connection, chalcogenide olivines have received less attention regarding the magnetism and magnetic excitations arising from their underlying sawtooth lattice. The A_2BX_4 (A = Mn, Fe, Ni; B = Si, Ge; X = S, Se, Te, O) olivines, where the A atoms form a sawtooth lattice, are well-known semiconducting magnetic compounds that find applications in optoelectronics and magnetic devices [16,17]. They have been recently computationally projected as suitable thermoelectric candidates owing to peculiar band structure features [18]. They crystallize in the orthorhombic *Pnma* space group and have relatively small tetrahedral ions (B) and large octahedral ions (A). Olivines have a spinel-like structure but use one quadravalent and two divalent cations $A_2^{2+}B^{4+}X_4$ instead of two trivalent and one divalent cations. The A sites consist of the two crystallographically independent sites (4*a* and 4*c* sites) and form a triangle-based sawtooth chain structure through the edge-sharing bonds along the *b* axis [19]. Due to this structural feature, the A-site lattice is geometrically magnetically frustrated when it is occupied by magnetic ions [19]. The end compounds of $Mn_2SiS_{4-x}Se_x$—Mn_2SiS_4 and Mn_2SiSe_4—order antiferromagnetically below their Néel temperature, $T_N \approx 83$ K and 66 K, respectively [20–23]. Mn_2SiS_4 belongs to the class of anisotropic uniaxial antiferromagnets but with anomalous magnetic features near the spin-flop transition [20]. A weak ferromagnetic interaction exists in a narrow temperature window between 83 K and 86 K, while displaying uniaxial anisotropy with the *b* direction as the easy axis. The origin of weak ferromagnetism (WF) and the unusual temperature dependence of the spin-flop critical field is unclear in olivines despite the microscopic origin of WF, which is supported by neutron scattering experiments [21].

*saparov@ou.edu
†hnair@utep.edu

At 4.2 K a collinear ferromagnetic arrangement of the Mn spins at the two distinct crystallographic positions, 4*a* (a site with inversion) and 4*c* (mirror), was observed along the *b* axis. As the temperature increases to 83 K, the orientation of the 4*a* spins turns in the *ab* plane. At 83 K, both the 4*a* and the 4*c* spins reorient along the *a* axis but with some canting in the *ac* plane. It is in the very small temperature range of 83–86 K that spins at two different crystallographic positions display weak ferromagnetism. The paramagnetic to antiferromagnetic transition has been identified as belonging to the Heisenberg universality class and the weak ferromagnetic transition as first order with a latent heat ≈ 0.01 J/mol [24]. A very low value of magnetic entropy, about 5% of $R\ln(2S+1)$, is found to be released at the antiferromagnetic transition, indicating that the spin entropy is not completely removed at the T_N. Experimental support for the short-range spin fluctuations comes from the fact that purely magnetic intensity was observed in neutron diffraction data up to 140 K [21].

On the other end of the composition series of $Mn_2SiS_{4-x}Se_x$ is the case of Mn_2SiSe_4, which has the magnetic easy axis along the crystallographic *c* direction of the orthorhombic cell [23]. In the case of Mn_2SiSe_4, the average magnetic structure remains in a configuration intermediate to a ferrimagnet and an antiferromagent for most of the $T < T_N$ region. Though both Mn_2SiS_4 and Mn_2SiSe_4 are reported to show similar magnitude of magnetization, Mn_2SiSe_4 displays pronounced field and temperature cycling dependencies in magnetic susceptibility [23]. The temperature range spanned by the magnetization maximum (between 66 K and 17 K, almost 50 K) is much wider compared to that of Mn_2SiS_4 (between 86 K and 83 K, approximately 3 K) [22,23]. The broadness of the transition in magnetic susceptibility of Mn_2SiSe_4 and the hysteresis-like effects already suggests strongly competing interactions leading to a frustrated magnetic state. An interesting aspect of the olivines that has recently received attention is related to thermoelectricity. Quasiflat-band edges near the valence and conduction bands were predicted using density functional theory calculations in the case of Fe_2GaCh_4 (Ch = S, Se, Te) [18]. This theoretical investigation was preceded by experiments that showed that nanostructured Fe_2GeS_4 is a photovoltaic material [16,25]. Experimental studies have shown that Fe_2SiS_4 and Fe_2GeS_4 possess significant thermopower [26].

In the present paper we undertake a detailed experimental study of magnetism in $Mn_2SiS_{4-x}Se_x$. Our research is motivated by the prospect of understanding the role of magnetic frustration in the sawtooth lattice of Mn in the series of olivines as the transition metal environment is altered from sulfur-rich to selenium-rich. A detailed magnetic and thermal property investigation of $Mn_2SiS_{4-x}Se_x$ ($x = 0, 1, 2, 3, 4$) solid solutions is undertaken and is complemented with density functional theory calculations.

II. METHODS

A. Experimental techniques

Elemental Mn, Si, S, and Se (99.99%, Aldrich) were used as reactants to synthesize $Mn_2SiS_{4-x}Se_x$, $x = 0$–4. Stoichiometric amounts of these elements were weighed and mixed properly using a mortar and pestle before pelleting and loading into a 10 mm diameter quartz ampule in a N_2-filled glove box. The quartz tubes were flame-sealed under a dynamic vacuum with pressure less than 10^{-3} mTorr. The reaction mixtures were heated at 1000 °C for 24 hours then cooled to room temperature at a rate of 100 °C/h. To improve the phase purity and crystallinity, samples were re-ground, pelleted, and annealed under identical conditions as necessary. Room temperature powder x-ray diffraction (PXRD) measurements were performed on a Rigaku MiniFlex600 instrument with a D/tex detector using a Ni-filtered Cu-$K\alpha$ radiation (λ_1 : 1.540562 Å; λ_2 : 1.544398 Å). X-ray data collection experiments were performed at room temperature in the 10°–70° (2θ) range, with a step size of 0.02°. Data analysis was performed using the Rigaku PDXL software package. The collected data were fitted using the decomposition method (Pawley fitting) embedded in the PDXL package. For air stability studies, powder samples of all three compositions were left in ambient air for a period of 6 weeks. PXRD measurements were regularly performed during this period using the conditions described above. The specific heat, $C_p(T)$, of the samples was measured using the heat pulse method in a commercial VersaLab physical property measurement system from Quantum Design. Tiny pellets of $Mn_2SiS_{4-x}Se_x$ of mass approximately 2–3 mg were used for the measurements. The sample was attached to the calorimeter puck using N Apiezon grease. The $C_p(T)$ was measured in the temperature range 50–300 K under 0 and 3 T. The temperature and field-dependent magnetization measurements were performed in a SQUID magnetic property measurement system. The dc magnetization was measured in the temperature range 2–300 K and isothermal magnetization at 2 K in the range –7 to 7 T. The thermal conductivity was measured using the TTO option in a commercial DynaCool-9 physical property measurement system from Quantum Design.

B. Computational methods

The density functional theory (DFT) calculations were carried out using the Vienna *ab initio* simulation package (VASP) [28–31]. The projector augmented wave (PAW) method was utilized for the electron-ion interaction [32–34] with an energy cutoff of 470 eV for the plane-wave basis functions. The generalized gradient approximation to the exchange-correlation functional by Perdew, Burke, and Ernzerhof [35] was used. A Γ-centered ($4 \times 4 \times 4$) k-point grid based on a Monkhorst-Pack scheme [36] was employed for initial structure optimization and later a finer grid of $6 \times 11 \times 13$ was used for further refinement. We relaxed the structures until the Hellmann-Feynman forces on the ions were lower than 0.04 eV/Å. An initial spin moment of 5 μ_B to Mn ions was assigned and the spin moment was allowed to relax. We also used the VESTA [27] software package for generating the crystal structures.

III. RESULTS AND DISCUSSION

A. X-ray diffraction and air stability

Powder x-ray diffraction (PXRD) patterns along with the Pawley fitting of $Mn_2SiS_{4-x}Se_x$ ($x = 0$–4) compounds

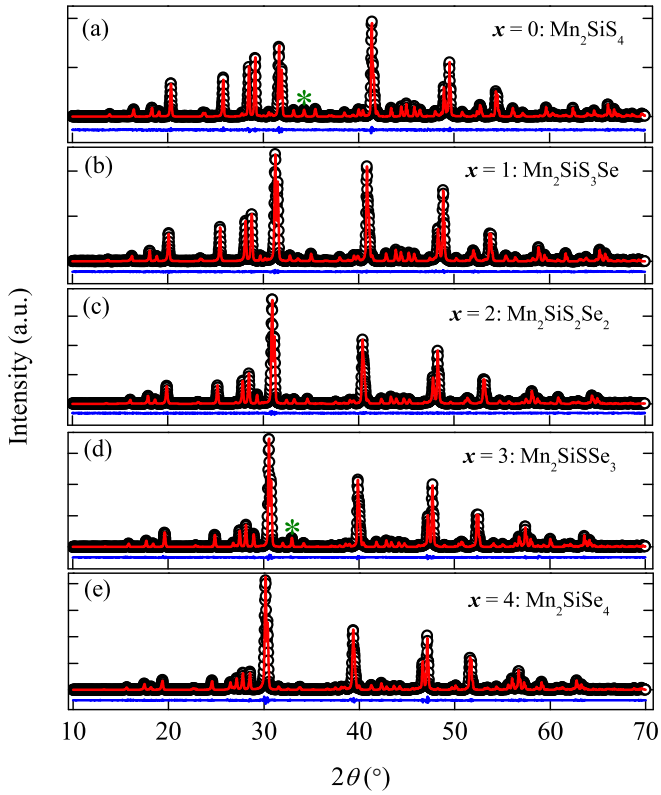

FIG. 1. (a)–(e) The PXRD patterns of $Mn_2SiS_{4-x}Se_x$ ($x = 0$–4) compositions are presented along with the results of structural analysis using the *Pbnm* space group. The black markers represent experimental data and the red lines are the fit using the Le Bail approach. The blue horizontal line shows the difference curve. In (a) and (d), an asterisk marks a minor impurity phase, α-MnS (≈2 wt. %).

measured at room temperature are shown in Fig. 1. The results of the structural analysis of the PXRD patterns are summarized in Table I. All samples crystallize in the orthorhombic *Pbnm* space group (No. 62). The compounds Mn_2SiS_3Se ($x = 1$), $Mn_2SiS_2Se_2$ ($x = 2$), and Mn_2SiSe_4 ($x = 4$) were obtained as pure-phase samples, whereas the Mn_2SiS_4 ($x = 0$) and Mn_2SiSSe_3 ($x = 3$) samples contained a minor impurity phase of α-MnS quantified to be less than 2 wt. %.

TABLE I. The lattice parameters, the goodness-of-fit parameter (R_{wp}), and χ^2 for the $Mn_2SiS_{4-x}Se_x$ compounds at 300 K. All compositions crystallize in the orthorhombic *Pbnm* space group.

	a (Å)	b (Å)	c (Å)	R_{wp} (%)	χ^2
Mn_2SiS_4	12.692(9)	7.435(3)	5.941(3)	3.94	2.89
Mn_2SiS_3Se	12.860(1)	7.527(4)	6.009(8)	2.48	1.23
$Mn_2SiS_2Se_2$	13.000(3)	7.605(6)	6.076(5)	2.31	1.42
Mn_2SiSSe_3	13.150(8)	7.690(9)	6.156(1)	1.78	1.35
Mn_2SiSe_4	13.302(8)	7.777(2)	6.243(6)	1.97	1.4
	d_{Mn-S} (Å)	d_{Si-S} (Å)		d_{Mn-Mn} (Å)	
Mn_2SiS_4	2.5616(4)	2.193(4)		3.9112(3) × 2	
	2.6391(5)	2.0375(3)		3.7169(6)	
	2.6226(5)			4.787(9) (along c)	
Mn_2SiSe_4	2.7034(4)	2.298(4)		4.0997(5) × 2	
	2.7513(1)	2.3118(6)		3.8876(4)	
	2.7403(9)			4.7153(6) (along c)	

Air stability of $Mn_2SiS_{4-x}Se_x$ is a very important feature while considering use in practical device applications. Being a nonoxide, many chalcogenide-based materials are prone to degradation upon exposure to air and moisture [37–39]. Air stability of $Mn_2SiS_{4-x}Se_x$ compounds was investigated for over a period of 6 weeks by keeping the powder sample exposed to the ambient atmosphere. PXRD was collected regularly during this period and analyzed. PXRD patterns of the as-synthesized samples and those of the samples after exposure to air for 6 weeks showed no appreciable differences (not shown). After a 6-week exposure to air, no additional peaks or peak broadening was observed in any of the five compositions. We confirm that Mn_2SiSe_4 series have good air stability thereby establishing their potential for use in practical applications.

The important structural feature of the $Mn_2SiS_{4-x}Se_x$ compounds from the perspective of magnetism is the sawtooth-like triangular arrangement of the Mn lattice [19]. Such a lattice forms the basis for a frustrated lattice depending on the different bond lengths or the exchange parameters related to the triangular motif building up the sawtooth. Mn has two crystallographically distinct positions in this structure, viz., 4*a* and 4*c*, where there are four magnetic ions per cell with inversion symmetry and mirror symmetry, respectively. Previous neutron powder diffraction studies on the $x = 0$ compound in the temperature range 4.2–300 K have shown that there is no structural change in the temperature range mentioned above. For all the $Mn_2SiS_{4-x}Se_x$ compounds, we assume the olivine structure in the entire temperature range employed in the present study. The refined lattice parameters that we obtain in the present study for Mn_2SiSe_4 match well with the earlier report on the crystal structure [40]. Incidentally, a structural peculiarity in which the Mn(1) octahedra is less distorted than the Mn(2) octahedra was mentioned in Ref. [40]. Similarly the lattice parameters obtained for Mn_2SiSe_4 series in the present work also match well with the reported values [22].

B. Specific heat

The experimentally measured specific heat of $Mn_2SiS_{4-x}Se_x$ ($x = 0$–4) is presented in Fig. 2(a), where the specific heats under 0 and 3 T are plotted together. The parent composition, Mn_2SiS_4, reproduces the antiferromagnetic phase transition at $T_N \approx 84$ K [20,24,41,42], which characterizes the paramagnetic-to-antiferromagnetic (PM-AF) phase transition. It is reported that in the temperature range 83–86 K, Mn_2SiS_4 displays WF; further, below 83 K it is an antiferromagnet. From the present $C_p(T)$ data of Mn_2SiS_4, we identify the AF transition at 86.2 K by taking the derivative, $dC_p(T)/dT$. The WF transition reported at 83 K is less conspicuous in our derivative plot (not shown). Under the application of 3 T magnetic field, no changes to the peak at T_N are noticeable for any of the compositions $x = 0$–4. This points towards strong AF nature of the underlying spin structure, up to at least 3 T. Upon substituting S with Se, the transition temperature T_N decreases from 86 K for $x = 0$

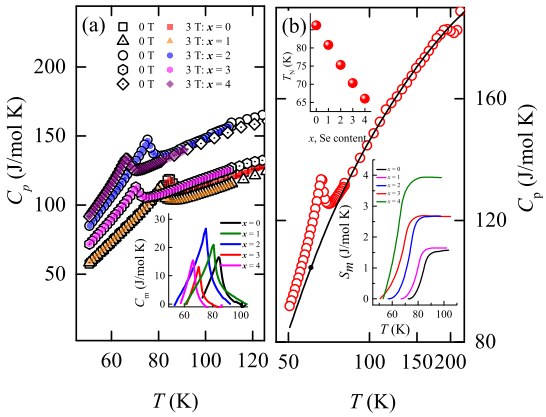

FIG. 2. (a) The specific heat of $Mn_2SiS_{4-x}Se_x$ ($x = 0$–4) obtained at 0 T and 3 T are plotted together, showing no significant influence of the external magnetic field on T_N. (b) Shows the $C_p(T)$ of Mn_2SiS_4 (red circles) along with the curve fit using the Einstein model (solid line). The inset of (a) shows the magnetic specific heat, C_m. The top inset in (b) shows that, with increasing x, the T_N decreases from 86 K to 66 K, while the entropy, S_m, is shown in the bottom inset. A significantly low value of entropy compared to $R\ln(2S+1)$ is released at the magnetic transition in $Mn_2SiS_{4-x}Se_x$ chalcogenides.

to 66 K for $x = 4$, for Mn_2SiSe_4. The evolution of T_N as a function of x is presented in the inset in panel (b) of Fig. 2.

In order to account for the phonon part of the specific heat of $Mn_2SiS_{4-x}Se_x$, an Einstein model-based curve fit was administered to the $C_p(T)$. We have used two separate Einstein terms and such a fit is demonstrated in Fig. 2(b) for the case of Mn_2SiS_4. In (b), the solid line represents the fit using the following expression:

$$C_{\text{Einstein}} = 3rR\sum_i a_i\left[x_i^2 e^{x_i}/(e^{x_i}-1)^2\right], \qquad (1)$$

where $x_i = \hbar\omega_E/k_BT$ and a_i is the weight factor for each mode. The specific heat data in the temperature range $T > 100$ K were used for the fit. We obtain the Einstein temperatures as $\theta_{E1} = 744$ K and $\theta_{E2} = 128$ K. The lattice part of the specific heat thus obtained was subtracted from the total specific heat to obtain the magnetic part, C_m, which is plotted in the inset of Fig. 2(a) for all the compositions of $Mn_2SiS_{4-x}Se_x$. The magnetic entropy, $S_m = \int(dC_m/T)dT$, is calculated and plotted in the inset of Fig. 2(b) for $x = 0$–4. Though the $Mn_2SiS_{4-x}Se_x$ compounds undergo a PM-AF second-order phase transition, it can be seen that significantly low magnetic entropy is released at the T_N. The Mn^{2+} with spin $S = 5/2$ contributes $R\ln(6) = 14.8$ J/(mol K) towards spin entropy. In the case of Mn_2SiS_4, only 14% of this value is released at the T_N. This, in turn, suggests that the Mn^{2+} spins of $Mn_2SiS_{4-x}Se_x$, which form a two-dimensional sawtooth-like triangular arrangement, are indeed in a frustrated magnetic state. Hence significant short-range magnetic order is expected to coexist along with the prominent AF order. It is noted here that the specific heat analysis that we have performed is on the data limited to only 50 K. Hence a comprehensive estimation of the lattice specific heat including a Debye term and extending down to low temperature was

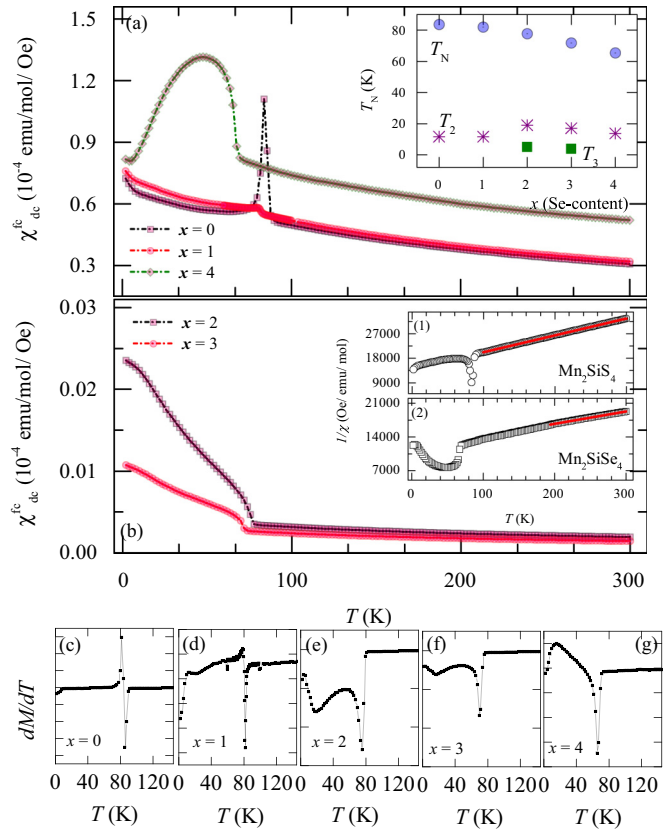

FIG. 3. The magnetic susceptibility of $Mn_2SiS_{4-x}Se_x$ ($x = 0$–4) obtained in 500 Oe field cooled conditions is presented for $x = 0$, 1, 4 in panel (a) and $x = 2$, 3 in panel (b). The inset of panel (a) shows T_N as a function of Se content (x). The insets (1) and (2) in panel (b) show the $1/\chi^{fc}_{dc}(T)$ curves of Mn_2SiS_4 and Mn_2SiSe_4, respectively, along with Curie-Weiss fit (red solid line). (c)–(g) The derivative dM/dT versus temperature showing the multiple anomalies present in each composition.

not possible. This would have resulted in a deviation in the values of S_m presented here. However, we obtain supporting values from the earlier reports on the specific heat analysis and magnetic entropy determination of Mn_2SiS_4 [24].

C. Magnetization

The dc magnetic susceptibility, $\chi^{fc}_{dc}(T)$, of the Mn_2SiSe_4 series measured in an applied magnetic field of 500 Oe is presented in Fig. 3 for $x = 0$, 1, 4 in panel (a) and $x = 2$, 3 in (b). Though the phase transition temperatures (T_N) identified in the specific heat data are reflected in magnetic susceptibility as well, a significant difference in the magnitude of magnetic susceptibility is observed for the two sets of compositions in panels (a) and (b). The magnetic phase transition in the case of Mn_2SiS_4 occurs as a sharp anomalous peak at $T_N = 83.7$ K and matches with the reported value [21,24]. Upon progressive replacement of S with Se, the peak at the phase transition is weakened, and eventually for Mn_2SiSe_4 a very broad feature is seen below ≈65 K. This observation also matches with the previous report of the magnetic behavior of Mn_2SiSe_4 [22]. The linear trend of decrease in the T_N

TABLE II. The magnetic transition temperatures (T_N), effective paramagnetic moment (μ_{eff}), and Curie-Weiss temperature (θ_{cw}) of different compositions of the $Mn_2SiS_{4-x}Se_x$ compounds. The T_N are determined from the derivative of magnetic susceptibility.

	T_N (K)	T_2 (K)	T_3 (K)	μ_{eff} (μ_B/Mn)	θ_{cw} (K)	$f = \frac{\lvert\theta_{cw}\rvert}{T_N}$	T_N/θ_{cw}	T_2/θ_{cw}	T_3/θ_{cw}
Mn_2SiS_4	83.7	11.7		4.0(3)	−226	2.7	0.36	0.05	
Mn_2SiS_3Se	81.9	11.7		4.07(2)	−221	2.7	0.36	0.05	
$Mn_2SiS_2Se_2$	77.7	19	5	3.95(5)	−219	2.8	0.35	0.08	0.02
Mn_2SiSSe_3	71.7	17	3.8	3.8(2)	−193	2.7	0.36	0.08	0.02
Mn_2SiSe_4	65.5	13.7		5.9(4)	−336	5.2	0.19	0.04	

can be connected to the covalent radius difference between S (1.05 Å) and Se (1.20 Å) [43].

The inset of (a) shows the T_N values estimated from the $\chi^{\text{fc}}_{\text{dc}}(T)$ data by taking the derivative, $\mathrm{d}\chi^{\text{fc}}_{\text{dc}}(T)/dT$. The derivative dM/dT as a function of temperature for $x = 0$–4 is presented in panels (c) to (g). The magnetic transition temperatures, T_N's, thus estimated through the derivatives are collected in Table II. From the magnetization data, we have been able to identify multiple magnetic anomalies at low temperatures for all the compositions in $Mn_2SiS_{4-x}Se_x$. For the $x = 0$, 1, and 4 compositions, in addition to the T_N, a low-temperature anomaly is observed in the temperature range near 12 K (denoted as T_2 in the table). For the $x = 2$ and 3 compositions, we observe two more anomalies T_2 and T_3 in addition to the T_N. This points out that the magnetic structure and the low-temperature magnetism of $Mn_2SiS_{4-x}Se_x$ compounds are more complex than the PM-AF-WF transitions that were reported earlier [20,22,24]. The presence of α-MnS found in two of the samples through x-ray diffraction analysis does not influence the magnetism as α-MnS has a magnetic transition at $T = 140$ K but we do not observe any anomalies at this temperature in any of the compositions. The effective paramagnetic moment, μ_{eff}, and the Curie-Weiss temperature, θ_{cw}, are estimated form the inverse magnetic susceptibility versus temperature data following a curve fit to the Curie-Weiss law. The insets (1) and (2) in panel (b) shows the representative Curie-Weiss fits administered on Mn_2SiS_4 and Mn_2SiSe_4 as red solid lines. The estimated parameters from the fit are collected in Table II for all five compositions. Slightly diminished values of effective moment compared to the theoretical spin-only moment of Mn^{2+} in the d^5 state, $\mu_{th} = 5.92\ \mu_B$, is observed in all the compounds except for Mn_2SiSe_4. The Curie-Weiss temperature returns negative values, which indicates that the overall magnetic interactions in these compounds are of antiferromagnetic type. The frustration parameter, $f = \frac{|\theta_{cw}|}{T_N}$, shows a value of nearly 2.7 for all the compositions except for Mn_2SiSe_4, for which a higher value of 5.2 is recovered. This indicates that the compound Mn_2SiSe_4 is significantly more frustrated than the other compounds. The frustration in $Mn_2SiS_{4-x}Se_x$ stems from the geometrical triangular sawtooth-like arrangement of Mn^{2+} spins. The value of f obtained for Mn_2SiS_4 compares well with the value reported for this material earlier [20]. The magnetic frustration effect that is observed through the frustration index f is supported by the structural feature of the triangular Mn arrangement (refer to Fig. 4) that makes up the sawtooth-like lattice. In the case of Mn_2SiS_4, which has $f = 2.7$, the Mn triangle has two equal distances, 3.97 Å, and one 3.71 Å. However, in the case of Mn_2SiSe_4, which has a high f value (5.2), the Mn triangle has all equal distances, 2.84 Å.

The magnetic structure of the $x = 0$ and 4 compounds, Mn_2SiS_4 and Mn_2SiSe_4, have been elucidated through neutron powder diffraction methods [21,23,24]. The neutron diffraction study of Mn_2SiS_4 confirmed the presence of olivine crystal structure in the whole temperature range of 4.2 K to 180 K. However, as noted previously, Mn in this structure occupies two distinct Wyckoff positions, 4*a* and 4*c*. At 4.2 K, the Mn moments in both the positions were found to be collinear with the *y* axis. At higher temperature, the magnetic moment on the 4*a* site gradually rotates away from the *y* axis. Between 83–86 K, both the 4*a* and 4*c* moments tend to align along the *x* axis. However, the moments are subjected to canting in the *x*-*z* plane. A similar case of tendency for canting of the spins was observed in Mn_2SiSe_4 as well. However, in this case a clear signature of diffuse

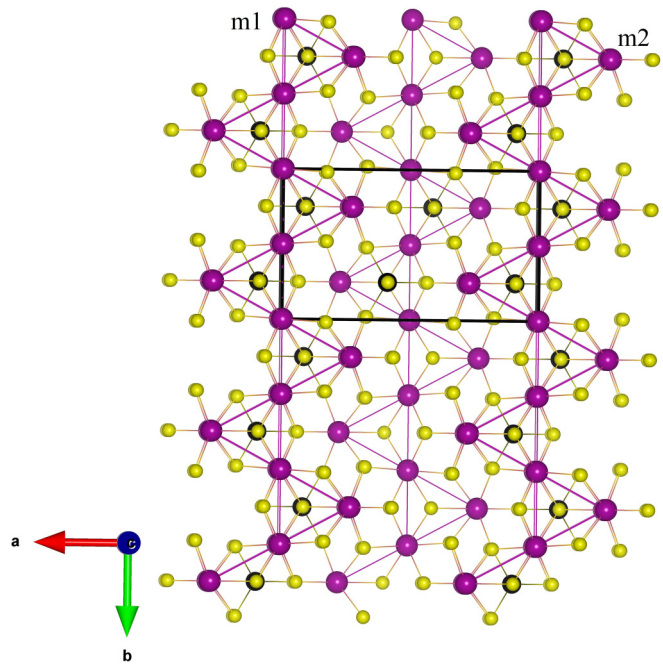

FIG. 4. A schematic of the olivine structure of Mn_2SiS_4. The unit cell is outlined in black solid line. The purple spheres are Mn. The sawtooth lattice formed by Mn^{2+} at the two crystallographically inequivalent sites m_1 and m_2 is shown. The line of m_1 atoms forms along the *b* direction. In the figure, the black spheres are Si and the yellow are S. The figure was created using VESTA [27].

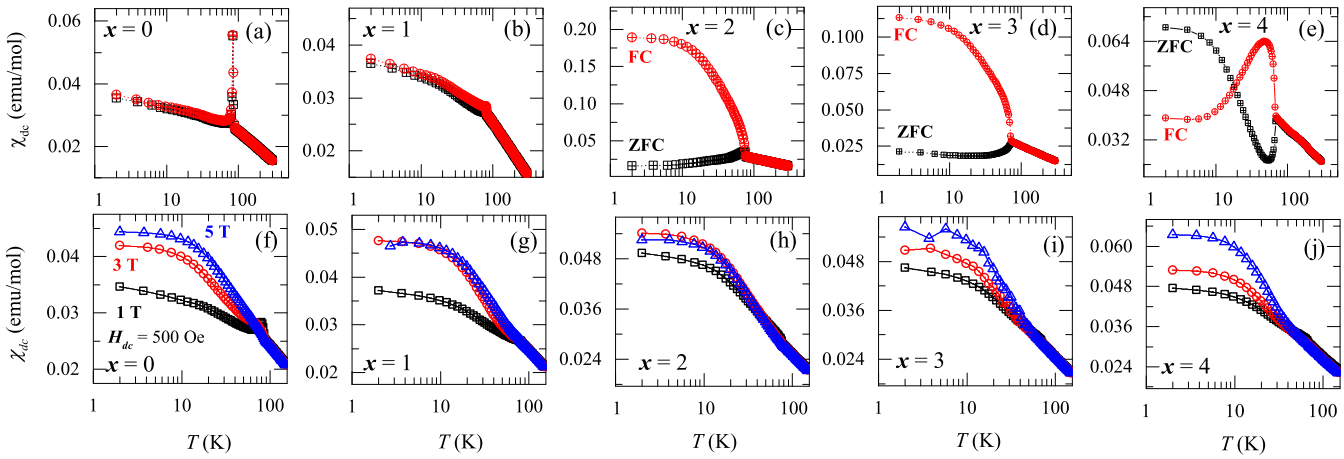

FIG. 5. (a)–(e) The dc magnetic susceptibility of $Mn_2SiS_{4-x}Se_x$ ($x = 0$–4) obtained in ZFC and FC protocol using an external field of 500 Oe. Large bifurcation in the ZFC and FC arms observed for $x = 2$, 3 whereas crossing of the ZFC and FC is seen for $x = 4$. (f)–(j) The dc susceptibility in field-cooled mode for 1 T, 3 T, and 5 T for $x = 0$–4. Even with the application of 5 T, no significant enhancement of magnetic moment is obtained.

magnetic scattering was observed, especially for the peaks at $2\theta = 22^\circ$ and 48° [23]. The magnetization of Mn_2SiSe_4 was then attributed to the short-range ferro- or ferrimagnetic arrangement of canted spins. The spin correlations as a part of the diffuse magnetic scattering is seen to persist up to 102 K. The observation to diffuse magnetic scattering in Mn_2SiSe_4 from the previous studies support the frustrated magnetism observed through a high frustration index, f, and also low magnetic entropy released at the T_N.

Multiple magnetic phase transitions at low temperature were observed in Mn and Fe orthosilicate olivines [44,45]. In $Mn_2SiS_{4-x}Se_x$ compounds, more than one magnetic anomaly is observed for all the compositions below their T_N (refer to Table II). By employing a Weiss mean-field model, the magnetic transitions in the Mn and Fe orthosilicates were qualitatively understood based on the parameter γ/α, which is the ratio of the two superexchange angles present in the spin structure of these magnets. The ratio γ/α compares to the ratio T_N/θ_{cw}. It was shown that in the special case where $2 < \gamma/\alpha < 1$, there arises a new low-temperature phase transition below T_N and it is indicated by the low values of the ratio T_2/θ_{cw}, where $T_2 < T_N$ is the low-temperature transition. In Table II, we have collected the ratios T_N/θ_{cw}, T_2/θ_{cw}, and T_3/θ_{cw} for the $Mn_2SiS_{4-x}Se_x$ compositions. It is easily noted that the value of T_N/θ_{cw} is relatively constant across the compositions, except for the highly frustrated composition, Mn_2SiSe_4. Also, the values of T_2/θ_{cw} and T_3/θ_{cw} are highly diminished compared to that of T_N/θ_{cw}. This is in agreement with the simple Weiss-field approach, where the calculated exchange energies supported the low-temperature magnetic anomalies. The broadness of the magnetic anomalies below T_N in the Mn_2SiSe_4 compositions points towards short-range magnetic order rather than long-range magnetic order in a new magnetic structure. The dc magnetic susceptibility of the $Mn_2SiS_{4-x}Se_x$ series in the zero-field-cooled (ZFC) and field-cooled (FC) protocol in the presence of external magnetic field, $H_{app} = 500$ Oe, is presented in Figs. 5(a)–5(e). The effect of external magnetic fields 1 T, 3 T, and 5 T on the field-cooled magnetic susceptibility is shown in panels (f)–(j) of the same figure. For the compositions $x = 0$, 1, the ZFC and the FC arms show no bifurcation at all [panels (a), (b)]. The magnetic phase transition is evident as a strong anomaly, thereby confirming the AFM transition. For the compositions $x = 2$, 3, and 4 strong irreversibilities are observed in the magnetic response which is an indication of significant short-range magnetic correlations or spin-glass-like features. Interestingly, the highly frustrated compound Mn_2SiSe_4 presents a ZFC/FC response in which the ZFC and FC arms cross each other in the low-temperature region. This crossing happens at $T \approx 18$ K. This feature resembles the case of negative magnetization observed in many other oxide systems [46–48]. In the case of the spinel compound Co_2VO_4, the negative magnetization was explained in terms of a ferrimagnetic structure ($T_c = 158$ K) and the resulting complex magnetism at low temperature. However, the presence of ferromagnetic clusters embedded in an AFM matrix also can display negative magnetization as evidenced in the case of the rare-earth manganite $NdMnO_{3\pm\delta}$, where the stoichiometry of the oxygens also seems to play a role [47]. In order to accurately determine the presence of ferromagnetic short-range-ordered clusters, low-temperature neutron diffraction experiments were undertaken. In the case of Mn_2SiSe_4, the magnetic structure that has been proposed already point towards the presence of short-range ferro- or ferrimagnetic arrangement of canted spins. The magnetization data presented in Fig. 5(e) support the claim of short-range ferrimagnetic canted spins. However, a detailed low-temperature neutron powder diffraction study can shed more light on the proposed magnetic features. It can be noted that the application of external magnetic fields up to 5 T does not produce appreciable enhancement of the magnetization in any of the $Mn_2SiS_{4-x}Se_x$ compositions [panels (f)–(j)].

The magnetization data presented in Figs. 3 and 5 clearly support a scenario of short-range magnetic order related to the spin fluctuations in the antiferromagnetic state. Though there is a definite role played by geometric frustration on the sawtooth lattice, it can be understood that magnetic anisotropy is also a key parameter that needs to be taken into account. Strong anisotropy effects in the magnetic response have

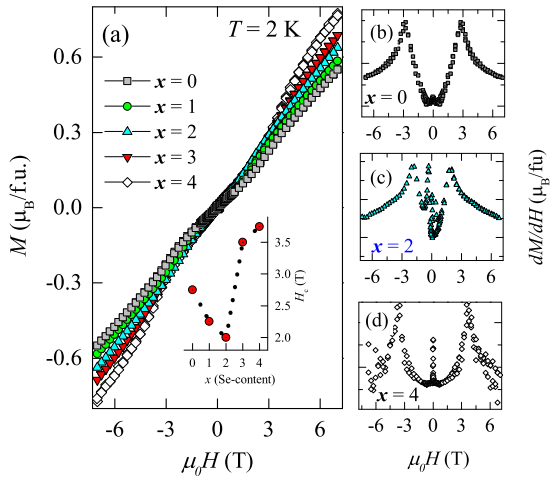

FIG. 6. (a) The isothermal magnetization of $Mn_2SiS_{4-x}Se_x$ (x = 0–4) at 2 K. The inset shows the evolution of the critical field, H_c, as a function of Se content, x. (b)–(d) The derivative dM/dH versus temperature showing the presence of metamagnetic phase transitions.

been reported in single crystals of Mn_2SiS_4 evidenced by the metamagnetic-like spin-flop transition [20]. Notably, the spin-flop critical field was found to decrease and vanish at the antiferromagnetic transition temperature in the case of Mn_2SiS_4. The present study, which is performed on polycrystalline samples, reveals the metamagnetic-like features in magnetization isotherms, thereby underlining the importance of anisotropy. Detailed torque magnetometry studies on single crystals of low-dimensional magnets have revealed the magnetocrystalline anisotropy effects in spin reorientation [49]. The $S = 1/2$ sawtooth chain in $Cu_2Cl(OH)_3$ is a recent example of a similar lattice where anisotropy effects were observed in magnetization and magnetostriction, under the application of high magnetic fields [50].

The isothermal magnetization curves, $M(H)$, as a function of applied field H in the range −7 T to +7 T at 2 K for $Mn_2SiS_{4-x}Se_x$, x = 0–4, are plotted together in Fig. 6(a). The curves represent a typical antiferromagnetic response with no indication of magnetic hysteresis. At 2 K and 7 T, the maximum magnetic moment attained is about 0.77 μ_B/f.u. for Mn_2SiSe_4. The lowest moment is attained for Mn_2SiS_4, which has a value of 0.55 μ_B/f.u. One of the earliest works on the Mn-chalcogenide olivines was related to the spin-flop transition and the associated tricritical point in the H-T phase diagram [20]. The field-induced spin-flop transitions are reproduced in all the compositions in the present series of Mn_2SiSe_4 (x = 0–4). The field-induced spin-flop transitions are clearly evidenced in the derivatives dM/dH versus $H(T)$ plotted in Figs. 6(b)–6(d), which are shown for x = 0, 2, and 4. The variation of the critical field H_c for spin flop as a function of the Se content is presented in the inset of (a). The spin-flop transition in Mn_2SiS_4 single crystals along the crystallographic c axis is observed at a critical field of about 3 T. In the present case, our samples of polycrystalline Mn_2SiS_4 also display the spin-flop transition at a comparable field value of 2.7 T. It can be observed that the H_c first decreases with the replacement of S with Se, until $x = 2$. Beyond $x = 2$, for $x = 3$, 4, H_c increases and reaches a maximum for Mn_2SiSe_4, which is in fact the highly frustrated composition in this group. In order to correlate the crystal and the electronic structure of the $Mn_2SiS_{4-x}Se_x$ and to explore the band structure peculiarities of the current compositions as compared to those observed in Fe-based olivines that are predicted thermoelectrics [18], we now take a look at the results from density functional theory calculations.

D. Density functional theory and thermal conductivity

The magnetic structures of Mn_2SiS_4 and Mn_2SiSe_4 are reported in the antiferromagnetic structure through neutron diffraction studies [21,23]. The magnetic moments of Mn are proposed to lie in the c direction; the spins in the ab plane are ferromagnetically coupled while the adjacent layers are coupled antiferromagnetically. We have performed the DFT calculations for the antiferromagnetic spin arrangement of the four different compositions in $Mn_2SiS_{4-x}Se_x$. The experimental crystal structure for Mn_2SiS_4, obtained from the room temperature structure determined in the present work, was used as the starting point to generate the initial structures for all four compounds following an energy-minimization process. The crystal symmetry is found to be orthorhombic with six inequivalent positions, agreeing with the $Pbnm$ space group reported [40]. The optimized lattice constants, spin magnetic moments, and band gaps of these systems are

TABLE III. The total energy (E_{AFM}), theoretical and experimental lattice parameters [$(a, b, c)_{th}$ and $(a, b, c)_{exp}$], magnetic moments (μ_t/Mn and μ_c/Mn), and calculated band gaps from the DFT calculations.

Composition	E_{AFM} (eV)	$(a, b, c)_{th}$ (Å)	$(a, b, c)_{exp}$ (Å)	μ_c/Mn (μ_B)	μ_t/Mn (μ_B)	Δ_b (eV)
Mn_2SiS_4	0.0	12.46, 7.27, 5.87	12.69, 7.44, 5.94	4.04, − 4.05	4.0	0.47
	0.40	12.69, 7.44, 5.94		4.12, − 4.16		0.64
Mn_2SiS_3Se (a)	0.34	12.726, 7.320, 5.892	12.860, 7.527, 6.009	4.03, − 4.03	4.07	
Mn_2SiS_3Se (b)	0.35	12.530, 7.315, 6.013		4.04, − 4.04		0.40
Mn_2SiS_3Se (1)	0.0	12.59, 7.35, 5.91		4.02, − 4.02		0.32
Mn_2SiS_3Se (2)	0.02	12.583, 7.335, 5.942		4.02, − 4.03		
Mn_2SiS_3Se (3)	0.12	12.590, 7.34, 5.96		4.04, − 4.02		
Mn_2SiS_3Se (4)	0.10	12.603, 7.338, 5.915		4.02, − 4.03		
$Mn_2SiS_2Se_2$	0.0	12.538, 7.432, 5.893	13.00, 7.61, 6.08	3.97, − 3.97	3.95	
Mn_2SiSSe_3	0.0	12.75, 7.45, 5.92	13.150, 7.690, 6.156	3.92, − 3.92	3.8	0.1
Mn_2SiSe_4	0.0		13.30, 7.78, 6.24	4.12, − 4.12	5.9	0.45

summarized in Table III and presented along with the corresponding experimental values for easy comparison. The total energy with the optimized lattice constants is lower than that with experimental lattice constants by 0.4 eV. The calculated magnetic moments on the Mn atoms show antiferromagnetic spin ordering. The DFT-calculated magnetic structure was found to match the experimental structure reported through previous neutron diffraction experiments [21]. The range of the calculated spin magnetic moments, μ_c, are presented in the table for the optimized structure. An agreement is found between the μ_c and the experimental values (μ_t) obtained from magnetization results of the present work. The substitution of one S by Se leads to two structures with the formula unit of Mn_2SiS_3Se, which are identified as structures (a) and (b) in Table III. Similar substitution by two Se atoms also leads to two structures using the same set of inequivalent atom position. Apart from these, we also tested mixed structures with random substitutional positions in a supercell which led to Mn_2SiS_3Se and $Mn_2SiS_2Se_2$ based on atom count only. However, we find that some of these structures have lower energy than the structures that conform to the orthorhombic symmetry and therefore we include them in the results, identified as structures Mn_2SiS_3Se (1)–(4) in Table III. For the $Mn_2SiS_2Se_2$ compound, substitution of inequivalent atoms leads to the lowest energy structure compared to random substitution and therefore we present only the lowest energy structure in the table. However, for this compound and for Mn_2SiSSe_3, random substitution can lead to low-lying structures within 0.02–0.07 eV above the ground state. The Mn_2SiSe_4 compound with experimental lattice parameters is the lowest energy structure. For all five compounds studied, the antiferromagnetic phase is the stable magnetic phase. The trend of the spin moment of the mixed compounds compares excellently with the trend seen from experiment. With higher number of Se atoms in the mixed compound, the spin moment decreases. However, the spin moment of the Mn_2SiSe_4 from DFT is much smaller compared to that derived from experimental data. We find that there can be several local minima in the potential energy surface with slightly different lattice constants for this compound. In all cases, however, the spin moment is still smaller than the experimental value. The experimental spin moments are determined from magnetization data collected at elevated temperatures, where lattice expansion can lead to reduced interactions between atoms. The DFT calculations are done without any temperature effect, which may explain the difference between the DFT and experimental spin moments. Moreover, these calculations also do not take into account noncollinear spin moments.

The band structures of the two terminal compounds Mn_2SiS_4 and Mn_2SiSe_4 are shown in Figs. 7(a) and 7(b), respectively. The band gap of Mn_2SiS_4 and Mn_2SiSe_4 was found to be 0.47 eV and 0.45 eV, respectively. Both structures have a direct band gap as indicated by the valence band maximum and conduction band maximum from the band structure plot. The band structures have flat bands from the G-X crystallographic direction and are similar to those of Gudelli *et al.* [18] in their Fe_2GeS_4 and Fe_2GeSe_4 band structure plots. The corresponding total and projected density of states (DOS) for Mn_2SiS_4 and Mn_2SiSe_4 is represented in panels (c) and (d) of Fig. 7. The DOS shows that the states

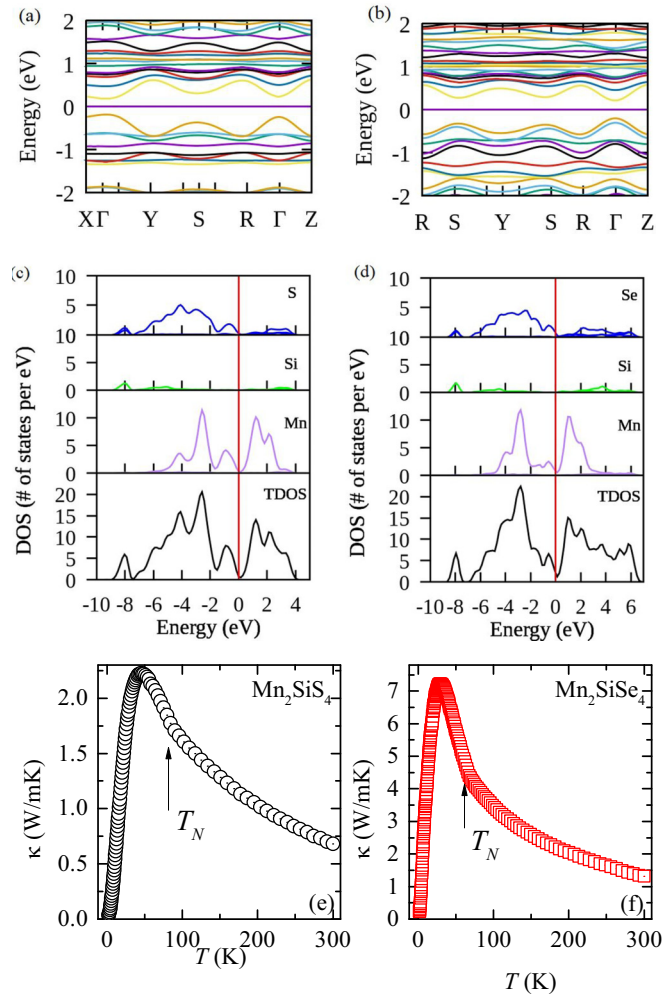

FIG. 7. The DFT-predicted band structure of (a) Mn_2SiS_4 and (b) Mn_2SiSe_4. The electronic projected density of states (PDOS) for Mn_2SiS_4 and Mn_2SiSe_4 is shown in (c) and (d), respectively. The experimentally measured thermal conductivity of (e) Mn_2SiS_4 and (f) Mn_2SiSe_4. The arrows mark the temperature of the antiferromagnetic phase transition.

near the Fermi level arise mainly from the Mn d states and S/Se p states. In both the systems the Si states lie deeper in energy. The conduction band has a contribution mainly from the Mn d states. The band gap obtained in the present study differs from that reported for Mn_2SiS_4 [51]. However, the antiferromagnetic spin arrangement assumed in the work by Davydova *et al.* seems to be different from the AFM structure that is obtained in the present work as well as in earlier neutron reports [21]. An LDA + U approach was used by Davydova *et al.*, which influences the band gap since U can be adjusted to match the experimental band gap.

Motivated by the band structure features that we found in Mn_2SiS_4 and Mn_2SiSe_4 and from the reports on other thiolivines that project these materials as potential candidates for thermoelectric applications, we measured the thermal conductivity, $\kappa(T)$. Figures 7(e) and 7(f) show the $\kappa(T)$ for Mn_2SiS_4 and Mn_2SiSe_4, respectively. Both compounds show thermal conductivity that is reminiscent of semiconducting materials where phonons dominate the thermal transport [52]. At

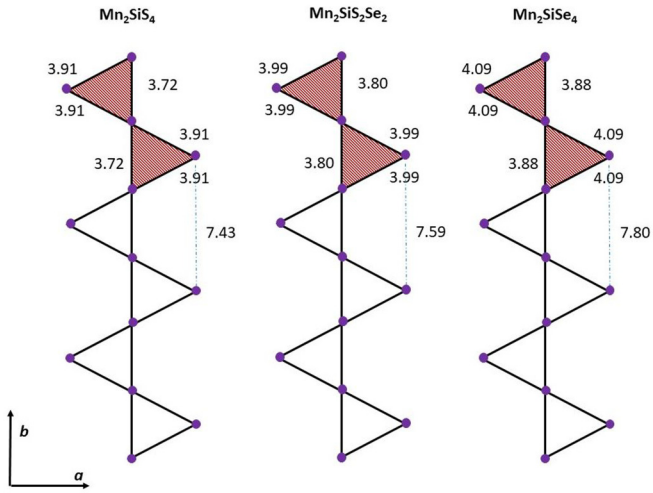

FIG. 8. A schematic figure showing the sawtooth chain of Mn in Mn_2SiS_4, $Mn_2SiS_2Se_2$, and Mn_2SiSe_4. The distance between Mn in the m_1 and m_2 positions is marked. The Mn triangles tend to form isosceles in all the $Mn_2SiS_{4-x}Se_x$ compositions. The distance between the 2-triangle units (shaded region) along the *b* direction increases as the Se content increases. The interlayer distances between the sawtooth layers (in the *ab* plane) also increase with higher Se content.

low temperatures the thermal conductivity rapidly increases with increasing temperature, forms a pronounced maximum centered below 50 K, and then decreases down to room temperature. The maximum in low temperatures occurs due to reduction of the thermal scattering at low temperatures, i.e., in the regime at which the phonon mean-free path becomes larger than the interatomic distances. For both compounds the magnetic phase transition appears only as a small kink in $\kappa(T)$ at the Néel temperature [marked by arrows in Figs. 7(e) and 7(f)]. The band gap obtained for Mn_2SiSe_4 is slightly diminished compared to that of Mn_2SiS_4, and the former shows *p*-type conductivity according to our Seebeck coefficient measurement (not shown).

As the Se content is increased from $x = 0$ to $x = 4$, the sharp magnetic transition observed in Mn_2SiS_4 is replaced with a broad transition extending over a large temperature range below 65 K. The results of the magnetization and specific heat experiments point towards the emergence of short-range order stemming from enhanced magnetic frustration. In Fig. 8 the Mn-Mn distances between the Mn atoms occupying the crystallographically distinct m_1 and m_2 positions are represented for Mn_2SiS_4, $Mn_2SiS_2Se_2$, and Mn_2SiSe_4. The distances marked on the figure are obtained from the refined x-ray diffraction data, which is cross-checked against the distances obtained from DFT. It can be seen from the figure that the Mn triangles that form the sawtooth lattice are isosceles and the Mn-Mn distances between the atoms in the m_1 chain (along *b*) increase with Se content. In general, the distances in the Mn triangle increase from Mn_2SiS_4 towards Mn_2SiSe_4. The Mn(m_1)-Mn(m_1) distance along the *c* direction for Mn_2SiS_4 is 5.94 Å, which increases to 6.24 Å for Mn_2SiSe_4. The Mn(m_1)-Mn(m_1) distances also undergo a similar increase. From this, it is clear that the interlayer distance between the sawtooth layers increases towards Mn_2SiSe_4 and subsequently a weakening of the exchange interaction can result. These structural features associated with the sawtooth triangles lead to the formation of spin clusters in $Mn_2SiS_{4-x}Se_x$ with increased Se content resulting in predominant short-range order.

IV. CONCLUSIONS

The magnetism of chalcogenide olivine $Mn_2SiS_{4-x}Se_x$ with a sawtooth lattice for the Mn moments is studied in detail using magnetization, specific heat, and first-principles density functional theory calculations. Progressive substitution of S using Se in Mn_2SiS_4 is seen to shift the antiferromagnetic transition temperature from 86 K to 66 K. Though an antiferromagnetic transition is clear, the magnetic entropy estimated from the analysis of specific heat reveals diminished values suggesting that strong spin fluctuations are present. Among the $Mn_2SiS_{4-x}Se_x$ compositions studied, Mn_2SiSe_4 is the most frustrated. A nonlinear trend in the evolution of the critical field for spin flop is found across the compositions. Density functional theory calculations support the stable orthorhombic crystal structure across the series and confirm the antiferromagnetic structure for Mn_2SiS_4 and Mn_2SiSe_4. Quasiflat-band features similar to those seen in Fe-based olivines are seen in the present case; however, the experimental thermal transport results do not support features favorable for a good thermoelectric.

ACKNOWLEDGMENTS

H.S.N. acknowledges the UTEP start-up fund and UT Rising-STAR in supporting this work. B.S. acknowledges the financial support for this work provided by the University of Oklahoma start-up funds. D.A. and K.G. acknowledge support from INL's LDRD and DOE's (Basic Energy Science) Early Career Research Programs, respectively. R.R.Z. and T.B. acknowledge support by Department of Energy Basic Energy Science through Grants No. DE-SC0002168 and No. DE-SC0006818. Support for computational time by the NSF's XSEDE project through Grant No. TG-DMR090071 is gratefully acknowledged. A.C. and S.R.S. acknowledge the University of Texas at El Paso (UTEP) start-up fund and the NSF-PREM program (DMR-1205302). The part of the paper prepared by S.R.S. and A.C. is funded under Award No. 31310018M0019 from UTEP and the Nuclear Regulatory Commission. The statements, findings, conclusions, and recommendations are those of the author(s) and do not necessarily reflect the views of UTEP or the US Nuclear Regulatory Commission.

[1] K. Kubo, Phys. Rev. B **48**, 10552 (1993).
[2] D. Sen, B. S. Shastry, R. E. Walstedt, and R. Cava, Phys. Rev. B **53**, 6401 (1996).
[3] T. Nakamura, and K. Kubo, Phys. Rev. B **53**, 6393 (1996).
[4] S. Blundell and M. Núñez-Regueiro, Eur. Phys. J. B **31**, 453 (2003).

[5] V. Ohanyan, Condens. Matter Phys. **12**, 343 (2009).
[6] S. Bellucci and V. Ohanyan, Eur. Phys. J. B **75**, 531 (2010).
[7] Z. Hao, Y. Wan, I. Rousochatzakis, J. Wildeboer, A. Seidel, F. Mila, O. Tchernyshyov *et al.*, Phys. Rev. B **84**, 094452 (2011).
[8] V. R. Chandra, D. Sen, N. B. Ivanov, and J. Richter, Phys. Rev. B **69**, 214406 (2004).
[9] M. E. Zhitomirsky and H. Tsunetsugu, Phys. Rev. B **70**, 100403(R) (2004).
[10] M. Zhitomirsky, Prog. Theor. Phys. Suppl. **160**, 361 (2005).
[11] X. S. Wang, H. W. Zhang, and X. R. Wang, Phys. Rev. Appl. **9**, 024029 (2018).
[12] R. Cava, J. Solid State Chem. **104**, 437 (1993).
[13] O. Le Bacq, A. Pasturel, C. Lacroix, and M. D. Nunez-Regueiro, Phys. Rev. B **71**, 014432 (2005).
[14] G. Lau, Phys. Rev. B **73**, 012413 (2006).
[15] J. S. White, T. Honda, K. Kimura, T. Kimura, C. Niedermayer, O. Zaharko, A. Poole, B. Roessli, and M. Kenzelmann, Phys. Rev. Lett. **108**, 077204 (2012).
[16] S. J. Fredrick and A. L. Prieto, J. Amer. Chem. Soc. **135**, 18256 (2013).
[17] J. K. Furdyna and J. Kossut, *Diluted Magnetic Semiconductors*, Semiconductors and Semimetals (Academic Press, New York, 1988), Vol. 25.
[18] V. K. Gudelli, V. Kanchana, and G. Vaitheeswaran, J. Phys.: Condens. Matter **28**, 025502 (2015).
[19] I. S. Hagemann, P. G. Khalifah, A. P. Ramirez, and R. J. Cava, Phys. Rev. B **62**, R771 (2000).
[20] K. Ohgushi and Y. Ueda, Phys. Rev. Lett. **95**, 217202 (2005).
[21] A.-M. Lamarche, G. Lamarche, C. Church, J. C. Woolley, I. P. Swainson, and T. M. Holden, J. Magn. Magn. Mater. **137**, 305 (1994).
[22] S. Jobic, F. Bode, P. Le Boterf, and G. Ouvrard, J. Alloys Compd. **230**, 16 (1995).
[23] F. Bodenan, V. B. Cajipe, G. Ouvrard, and G. Andre, J. Magn. Magn. Mater. **164**, 233 (1996).
[24] A. Junod, K.-Q. Wang, G. Triscone, and G. Lamarche, J. Magn. Magn. Mater. **146**, 21 (1995).
[25] B. I. Park, S. Yu, Y. Hwang, S. H. Cho, J. S. Lee, C. Park, D. K. Lee, and S. Y. Lee, J. Mater. Chem. A **3**, 2265 (2015).
[26] H. A. Platt, Ph.D. thesis, Copper and iron chalcogenides for efficient solar absorption (Oregon State University, 2010).
[27] K. Momma and F. Izumi, J. Appl. Crystallogr. **44**, 1272 (2011).
[28] G. Kresse and J. Hafner, Phys. Rev. B **47**, 558 (1993).
[29] J. Furthmüller, J. Hafner, and G. Kresse, Phys. Rev. B **50**, 15606 (1994).
[30] G. Kresse and J. Furthmüller, Comput. Mater. Sci. **6**, 15 (1996).
[31] G. Kresse and J. Furthmüller, Phys. Rev. B **54**, 11169 (1996).
[32] P. E. Blöchl, Phys. Rev. B **50**, 17953 (1994).
[33] G. Kresse and D. Joubert, Phys. Rev. B **59**, 1758 (1999).
[34] P. E. Blöchl, C. J. Först, and J. Schimpl, Bull. Mater. Sci. **26**, 33 (2003).
[35] J. P. Perdew, K. Burke, and M. Ernzerhof, Phys. Rev. Lett. **77**, 3865 (1996).
[36] H. J. Monkhorst and J. D. Pack, Phys. Rev. B **13**, 5188 (1976).
[37] A. Choudhury, S. Strobel, B. R. Martin, A. L. Karst, and P. K. Dorhout, Inorg. Chem. **46**, 2017 (2007).
[38] J. C. Flanagan and M. Shim, J. Phys. Chem. C **119**, 20162 (2015).
[39] A. de Kergommeaux, J. Faure-Vincent, A. Pron, R. de Bettignies, B. Malaman, and P. Reiss, J. Am. Chem. Soc. **134**, 11659 (2012).
[40] J. Fuhrmann and J. Pickardt, Acta Crystallogr. C **45**, 1808 (1989).
[41] K. Ohgushi and Y. Ueda, AIP Conf. Proc. **850**, 1277 (2006).
[42] K. Ohgushi and Y. Ueda, J. Magn. Magn. Mater. **310**, 1291 (2007).
[43] R. T. Shannon and C. Prewitt, Acta Crystallogr. B **26**, 1046 (1970).
[44] H. Kondo and S. Mlyahara, J. Phys. Soc. Jpn. **21**, 2193 (1966).
[45] R. Santoro, R. Newnham, and S. Nomura, J. Phys. Chem. Solids **27**, 655 (1966).
[46] A. Kumar and S. Yusuf, Phys. Rep. **556**, 1 (2015).
[47] F. Bartolomé, J. Bartolomé, and J. Campo, Phys. B (Amsterdam) **312-313**, 769 (2002).
[48] N. Menyuk, K. Dwight, and D. Wickham, Phys. Rev. Lett. **4**, 119 (1960).
[49] N. Novosel, W. Lafargue-Dit-Hauret, Ž. Rapljenović, M. Dragičević, H. Berger, D. Cinčić, X. Rocquefelte, and M. Herak, Phys. Rev. B **99**, 014434 (2019).
[50] L. Heinze, H. Jeschke, A. Metavitsiadis, M. Reehuis, R. Feyerherm, J.-U. Hoffmann, A. Wolter, X. Ding, V. Zapf, C. Moya *et al.*, arXiv:1904.07820.
[51] A. Davydova, J. Eriksson, R. Chen, K. Rudisch, C. Persson, and J. J. S. Scragg, Mater. Des. **152**, 110 (2018).
[52] T. M. Tritt, *Thermal Conductivity: Theory, Properties, and Applications* (Springer Science & Business Media, 2005).